ICAS Paper 80 - 4.4

EXPERIMENTAL STUDIES OF THE UPPER-SURFACE-BLOWING PROPULSION SYSTEM AT CRUISE*

J. A. Braden
Lockheed-Georgia Company
Marietta, Georgia

and

W. C. Sleeman
NASA-Langley Research Center
Hampton, Virginia

Abstract

In the interest of providing a high-speed experimental data base for upper-surface-blowing (USB) configurations, an extensive wind-tunnel evaluation of geometrically related powered nacelles has been undertaken.* The experimental studies encompassed both force-balance and surface-pressure testing of a matrix of closed-forebody nacelles mounted on the upper-surface of either a straight or 25°-swept wing. As representative of the cruise speed range, the tests were conducted in the Mach range of 0.60 - 0.80. The model nacelles were unrefined in the sense that no attempt was made to aerodynamically contour or integrate the wing/nacelle combination except through filleting. The nozzle test matrix included variations in nozzle exit aspect ratio, nozzle size, nozzle boattail angle and exit position location. Analysis of the test results have emphasized the effects of nozzle operating conditions on measured lift and drag and in particular, the composition of the incremental force changes with blowing rate. It is found that differences in jet-induced surface pressures can occur between static and wind-on conditions giving rise to an apparent cruise pressure drag component influenced by nozzle width and degree of jet attachment. For highly three-dimensional nozzle shapes (circular, "D-Duct") an optimum operating pressure ratio is indicated for minimum drag designs. A limiting boattail angle for the cruise nozzle is deduced providing a basis for nozzle design compromises satisfying both cruise and low-speed (high-lift) requirements.

1.0 Introduction

Integration of the primary propulsion system with the airframe in such a manner that favorable aero-propulsion interactions are promoted has been a major design objective in recent years. The upper-surface-blowing (USB) concept has received general industry endorsement in recognition of its favorable low-speed, high-lift and acoustic characteristics. There have been reservations, however, regarding the ability of the system to achieve competitive, high-speed cruise performance. In the interest of establishing a broad, experimental data base from which competitive USB cruise designs may possibly evolve, the Lockheed-Georgia Company, under contract to NASA-Langley*, undertook an extensive wind tunnel evaluation of the aerodynamic effects of geometric variables pertinent to these configurations. The basic objective of the experimental program was to utilize relatively unrefined model components, representing a broadly spaced configuration matrix, with which the sensitivity of cruise aerodynamics to nacelle geometric variations could be assessed. Therefore, in this initial phase, while minimum-drag USB designs were of obvious, ultimate interest in these studies, the intent of the subject program was to develop guidelines in terms of nacelle geometry and those potential design concepts from which the more competitive USB system could be realized. The present paper will describe the experimental program, and the process of data analysis and results for the derivation of geometry-related, USB aerodynamic effects at cruise.

2.0 Experimental Program

The experimental studies encompassed both force-balance and surface pressure testing of various nacelle-wing combinations over the Mach number range from 0.6 - 0.80. The model nacelles, Figures 1 and 2, were generally of symmetrical design utilizing closed forebodies with a 300 psia

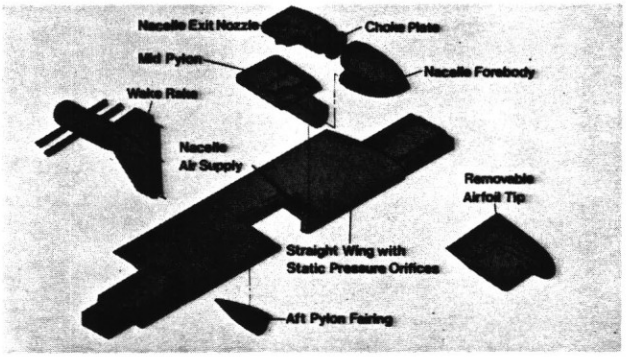

Figure 1. Exploded View of Basic Test Model Arrangement

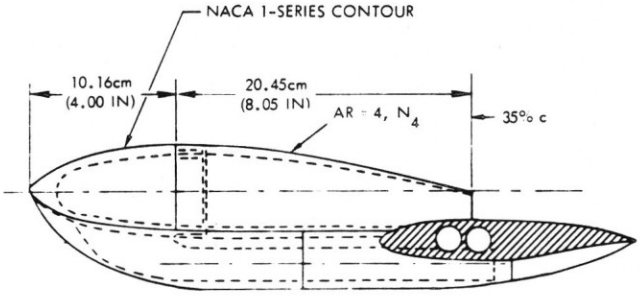

Figure 2. Nacelle General Arrangement for Straight Wing

*Research supported by NASA Contract NAS1-13871, "Exploratory Studies of Cruise Performance of Upper-Surface-Blown Configurations"; W. C. Sleeman, Contract Monitor, NASA, Langley.

air supply simulating the jet-efflux passing over the aft-wing surface. The nacelle test matrix included variations in nozzle exit aspect ratio (circular, semi-circular, or "D-Duct," 4 and 6), variations in nozzle size [wing chord^2/(nozzle exit area) = 24 and 48] and variations in nozzle boattail angle and exit locations. The nacelles were sized to the wing on the basis of current turbo fan-powered STOL designs through the parameter C^2/A_N. The medium-sized nacelles ($C^2/A_N = 24$) represented two-engine configurations whereas the $C^2/A_N = 48$ nacelles simulated four-engine aircraft. The nacelle geometric variations were studied as straight (unswept) wing/nacelle installations and as in combination with a 25-degree swept-wing (Figures 3 and 4). Both wings could be tested as either a semi-span force model or as a two-dimensional surface-pressure configuration. When used in the latter mode, a traversing wake-rake, shown in Figure 1, was employed to obtain spanwise wake profiles supplementing the surface-pressure data. The 7-inch chord wing sections were of a supercritical-type with thickness ratios of 16 percent (straight wing) and 14.5 percent (swept wing).

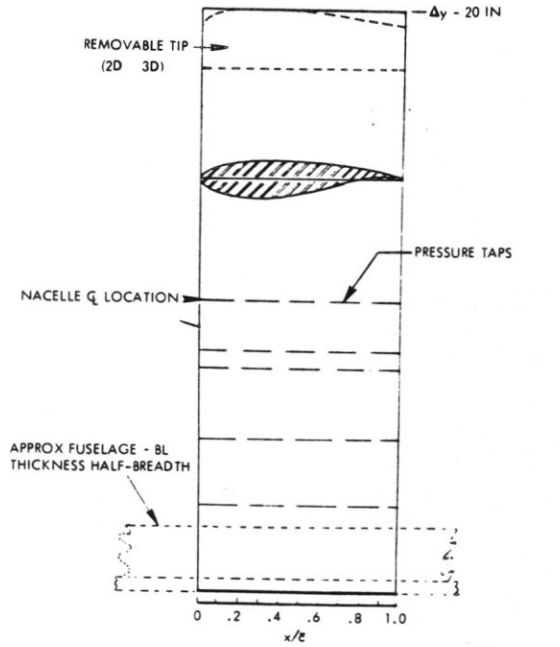

Figure 3 (a). Straight Wing, t/c = 0.16, Semi-Span = 20 In.

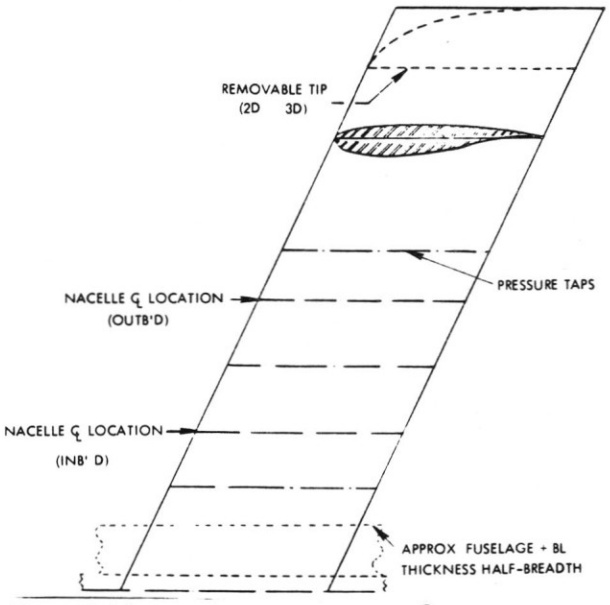

Figure 3 (b). Swept Wing, (λ c/4 = 25°) t/c = 0.145, Semi-Span = 20 Inches.

The tests were conducted in the Lockheed 20"×28"-wide compressible flow facility (CFF) with corroborative force testing performed in the Lockheed 4'×4' blow-down tunnel. The test Reynolds number, based on wing chord, was 3.5×10^6 and the nozzle blowing range was nominally $0 \leq H_j/P_\infty \leq 3.0$. All force-tests utilized a wall-type balance bridged by the nozzle air supply system with an opposing-bellows arrangement.

To extract thrust forces from the balance-measured drag data, the following relationship applies:

Measured Accel. Force	=	Total Config. Drags.	-	Isolated Nacelle Thrust

(i.e. Drag is A + Force) (1)

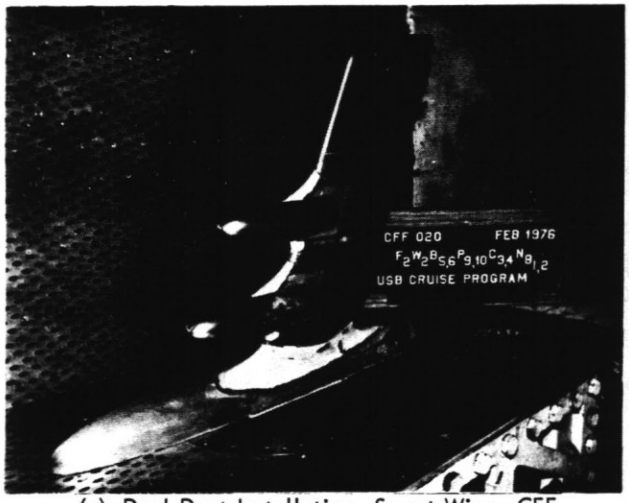

(a) Dual Duct Installation, Swept Wing, CFF

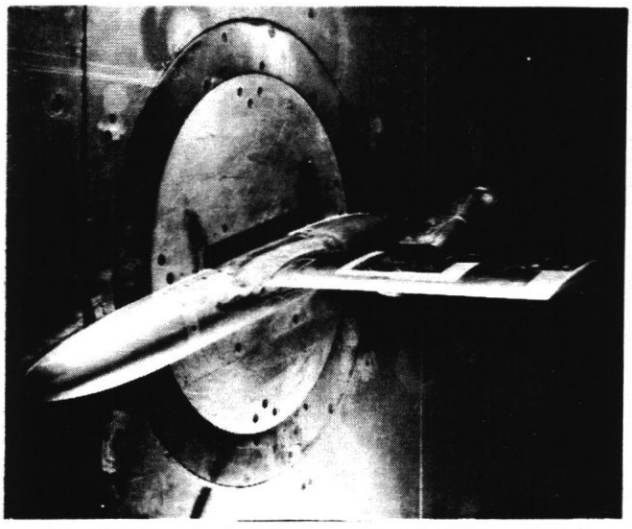

(b) AR4 Nozzle Installation, Straight Wing, 4' X 4'

Figure 4. Typical Semi-Span Test Configurations

Considerable effort was expended in assuring the accuracy of the thrust calibrations of the isolated nacelles. First, the nozzles were calibrated statically on a highly-sensitive balance system with total head rakes installed for surveying the nozzle exit flow. Secondly, the nozzles and wing/body were combined metrically with the test wall-balance, but with the nozzles located remotely from the wing-surface itself to prevent interaction between the wing and nacelle/jet. With this method of static calibration, air was supplied through the test-balance and model in a manner identical to that used for the wind-on tests. Comparisons between the two sets of calibrations, across the blowing range, provided a check on the accuracy of the bridged wall-balance as well as the stability of the air-flow within the internal supply passages of the model. A third set of static tests was conducted on all wing/nozzle combinations with the nozzles installed correctly on the wings. These test results, following established convention normally employed for high-lift testing, provided first-order levels of scrubbing losses $(1-\eta_T)$ and static jet-deflection angles, $(\delta_j)_s$ by force-vector summations. Figure 5 shows typical variations of these parameters with nozzle pressure ratio for a range of test

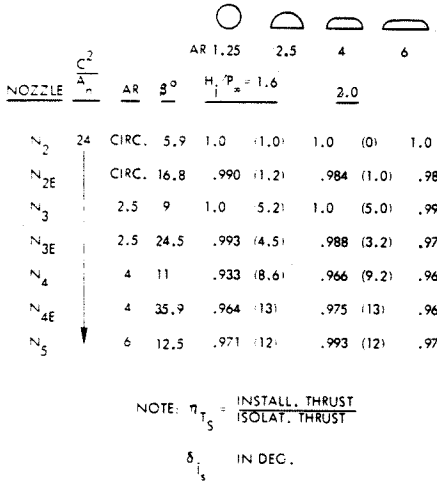

Figure 5. Tabulation of η_{T_S} (δ_{j_s}) For Test Nozzles; Static Data

configurations. The installed thrust losses relative to the isolated nacelle thrust, ranged from a maximum of 7 percent for the medium-sized, wide (aspect ratio 6) nozzles to less than 1 percent for the circular exit shapes. Corresponding maximum static jet deflection angles were about 12 degrees and 0 degrees, respectively, which may be compared to an upper-surface wing trailing-edge angle of about 16 degrees (straight wing) and 17 degrees (swept wing).

3.0 Test Data Analysis

Analysis of the force-data had the objective of identifying the components of total lift and drag increments associated with the blowing nacelle installations as well as the sources of these forces. Nacelle drag increments were derived by subtracting from the total measured configurational drag, equation (1), that drag associated with the wing-body alone at a constant, total lift coefficient, or:

$$\Delta C_{D_N} = \begin{bmatrix}\text{Meas. Accel.}\\ \text{or}\\ \text{Drag Force}\end{bmatrix} + \begin{bmatrix}\text{Isolated}\\ \text{Nacelle}\\ \text{Thrust}\end{bmatrix} - \begin{bmatrix}\text{Wing-}\\ \text{Body}\\ \text{Drag}\end{bmatrix} \quad (2)$$

$(at\ C_{L_{TOT}} = constant)$.

Figure 6 shows typical trends and magnitudes of nacelle drag increments as functions of lift and thrust coefficients for several representative test configurations. The Mach number of 0.68 is near the drag-rise of the straight wing/nacelle combination. At constant C_L, both cases are similar in that above the flow-through pressure-ratio $[(H_j/P_\infty) \simeq 1.40]$ a relatively weak drag minimum is indicated denoting a localized boundary layer control action of the jet on the aft-wing surface; this becomes more pronounced as wing lift increases. Beyond this "bucket," the drag increment rises sharply until the nozzle starts operating in the "hard-choke" condition $[(H_j/P_\infty) \geq 1.89]$ creating strong compression/expansion waves in the post-exit flow. Although the nozzle configurations in this instance produce relatively wide jets (i.e. in contrast to circular nozzles), the abrupt pressure fluctuations due to the presence of the waves inhibit jet-attachment up to the wing trailing edge. As a consequence, the jet tends to detach from the surface in the high blowing range with a subsequent drop in the drag increment level. Excursions from the nominal test matrix into the very high blowing range showed an almost cyclic variation in drag increment as the wave patterns moved progressively toward the trailing edge with increased jet exit velocity. Corresponding lift increments, given in Figure 7, at constant angles

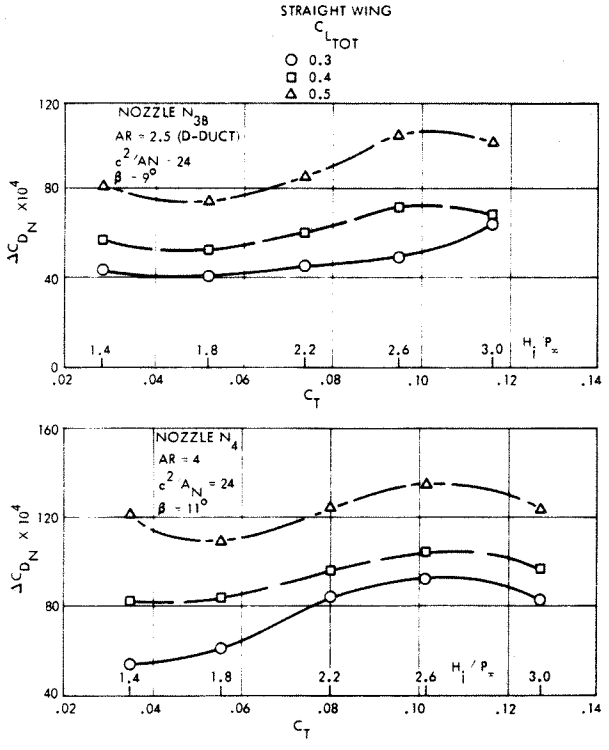

Figure 6. Effect of Lift Coefficient on Nacelle Drag, $M_\infty = 0.68$

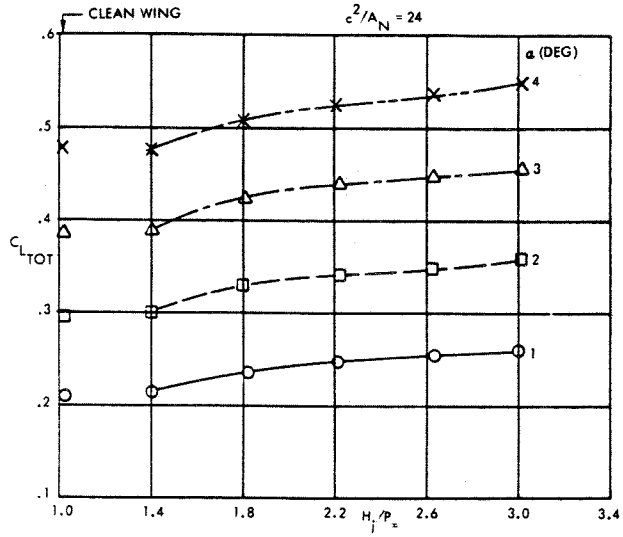

Figure 7 (a). Effect of Nozzle Pressure Ratio on Total Lift, noz N_{3_E}, AR = 2.5, $M_\infty = 0.68$

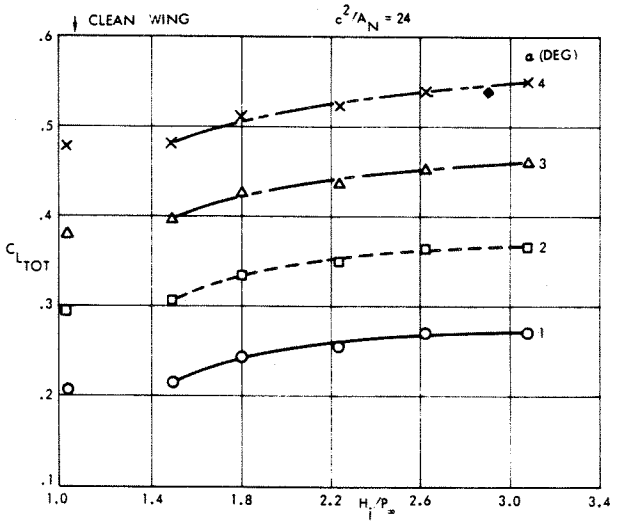

Figure 7 (b). Effect of Nozzle Pressure Ratio on Total Lift, noz N_{3_E}, AR = 4, $M_\infty = 0.68$

of attack, illustrate characteristic trends with thrust coefficient with an initial, rapid rise in lift followed by a gradual leveling off in the higher blowing range. These rather typical cases of lift and drag variations reflect a variety of aerodynamic effects which are responding primarily to the jet condition. To establish source-identification and establish trends and magnitudes of such effects, an attempt has been made to break the lift and drag down into the various elements accruing to the total increments using several basic assumptions.

Drag Increment Components

It is assumed that the total drag increment is composed of, but not limited to, the following components:

ΔC_{DNF} - skin friction drag coefficient of the basic nacelle

ΔC_D - scrubbing drag coefficient due to the jet flow

ΔC_{D_j} - pressure drag due to jet-induced effects

ΔC_{D_i} - coefficient of drag-due-to-lift

It was the objective of this phase of the study to quantify the foregoing elements using the force-test results, surface-pressure data, wake-rake profiles and static tests as the basis for such a breakdown.

Skin Friction Drag, ΔC_{DNF} - The skin friction drag coefficient was estimated for each nacelle configuration using conventional procedures; these were corrected for interfacing footprint areas between nacelle and wing. Figure 8 provides a tabulation of the final drag coefficients which amount to roughly $C_D = .0020 - .0025$ for a single, medium-sized nacelle $[(C^2/A_n) = 24]$ and about one-half of this range for the smaller nacelle, $[(C^2/A_n) = 48]$.

Scrubbing Drag, C_{D_η}. Thrust losses due to jet scrubbing were quantified by the assumption that the statically-derived parameter, $\eta_T = T_{Install}/T_{Isol}$, is applicable to wind-on conditions as well as the static case. There are obvious problems with this assumption if the foregoing rationale of significant variations in the degree of jet attachment and, thereby jet deflection and scrubbing at high blowing rates (wind-on), is valid. However, this assumption is used here on a first-order basis with the anticipation that any large variations in the actual wind-on value would become apparent in the subsequent rebuild-up to the measured drag increments. Accordingly, the scrubbing drag component is computed as:

$$\Delta C_{D_\eta} = C_T(1-\eta_T) \qquad (3)$$

where C_T is the gross-thrust coefficient of the isolated nacelle at various nozzle pressure ratios.

NOZZLE	c^2/A_N	AR	WING INSTALL.	$\Delta C_{D_{NF}}$
N_2	24	CIRC.	STRAIGHT WING	0.0022
N_{2E}		CIRC.		0.0023
N_3		2.5		0.0025
N_{3E}		2.5		0.0021
N_4		4		0.0024
N_{4E}		4		0.0020
N_5		6		0.0024
N_8	48	2.5	25° SWEPT WING	0.0012
N_{11}		CIRC.		0.0013
N_{12}		4		0.0014
N_{13}		6		0.0013
$N_8^1 + N_8^2$ (DUAL)		2.5		0.0024

Figure 8. Tabulation of Estimated Skin Friction Drag of Test Nacelles

Jet Pressure Drag, ΔC_{D_j}. As the jet turns through a deflection angle, δ_j, it generates pressures on the turning surface which can be componentized into the lift and drag directions. From momentum relationships, these can be written as:

$$\Delta C_{D_j} = \eta_T C_T [1 - \cos(\alpha + \delta_j)]$$
$$\Delta C_{L_j} = \eta_T C_T \sin(\alpha + \delta_j) \quad (4)$$

While the angle δ_j is known from static tests, at wind-on conditions it would be expected that injection of the jet into the existing aft-wing pressure-field could generate excess negative pressures through the cross-product terms associated with $(V_\ell + \Delta V_j)^2$. Figure 9 compares surface pressures along the jet centerline from a semi-circular "D-Duct" nozzle at both static and wind-on conditions. For convenience, the pressure coefficient has been nondimensionalized on jet dynamic pressure, q_j, for a fully-expanded jet rather than the freestream. Although, the strong shock formations ($H_j/P_\infty = 2.6$) obscure the effect to some degree, it is apparent from these and similar results, that the pressure level, wind-on, is substantially higher (more negative) than was found statically as would be expected. Additionally, the mean pressure level can exceed that manifested on the clean wing alone as shown in the figure. This difference can be interpreted as an increase in the effective wind-on jet angle from that determined statically. In fact, spanwise flow surveys along the wing trailing-edge using a laser velocimeter, Figure 10, also shows that the effective inclination of the trailing edge flow behind a small "D-Duct" nacelle is substantially higher for the wind-on case than was found statically. Further evidence of this is indicated in Figure 11 portraying results from a wake-rake survey behind a medium-sized "D-Duct" nozzle; the greater deflection of the jet at wind-on ($M_\infty = .68$), is apparent.

To consider further the possible magnitude of the effective jet-angle at wind-on conditions, it is of interest to integrate the surface pressures within the jet scrubbed area for comparison to the highly simplified predictions of equations (4). Before presenting these results, however, it should be noted that equation (4) can be redefined in terms of jet [or nozzle] height (h) and the

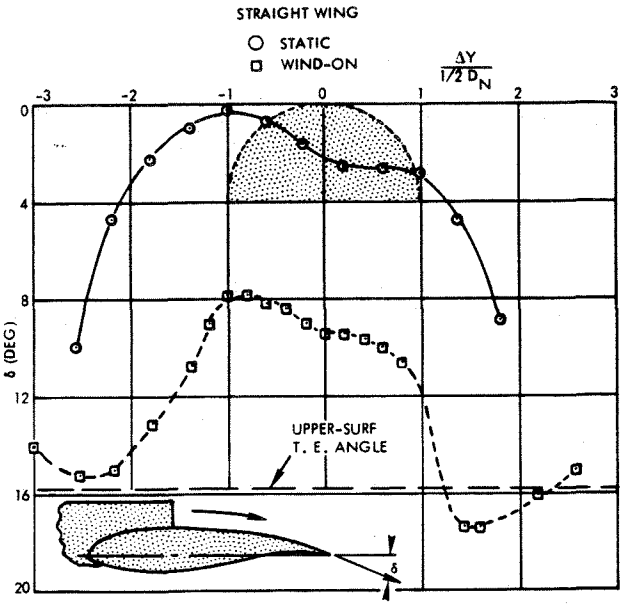

Figure 10. LV Measurements of Spanwise Distribution of Trailing-Edge Flow Angularity, Small "D-Duct" Nacelle, $\alpha = 0^\circ$

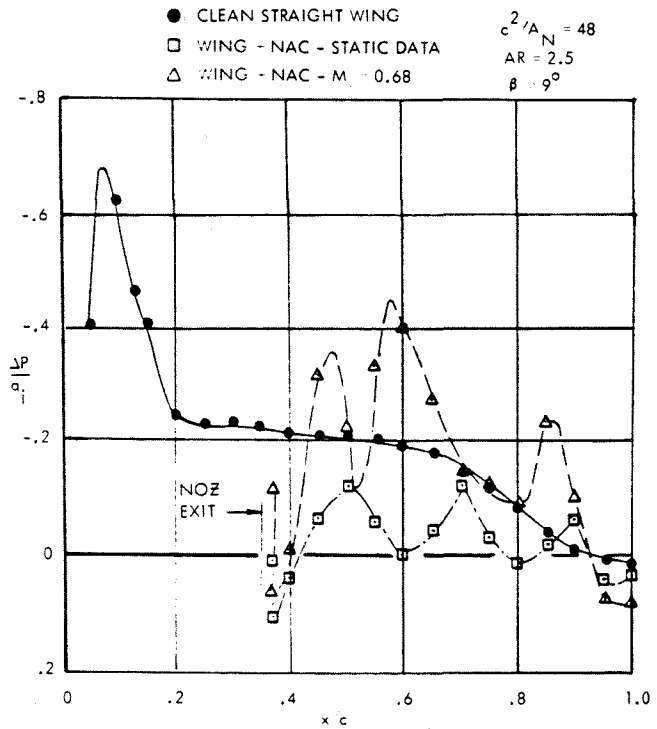

Figure 9. Jet-Centerline Pressure Distributions Behind Streamlined "D-Duct" Nozzles, N_6, $N_j/P_\infty = 2.6$, $\alpha = 2.6^\circ$

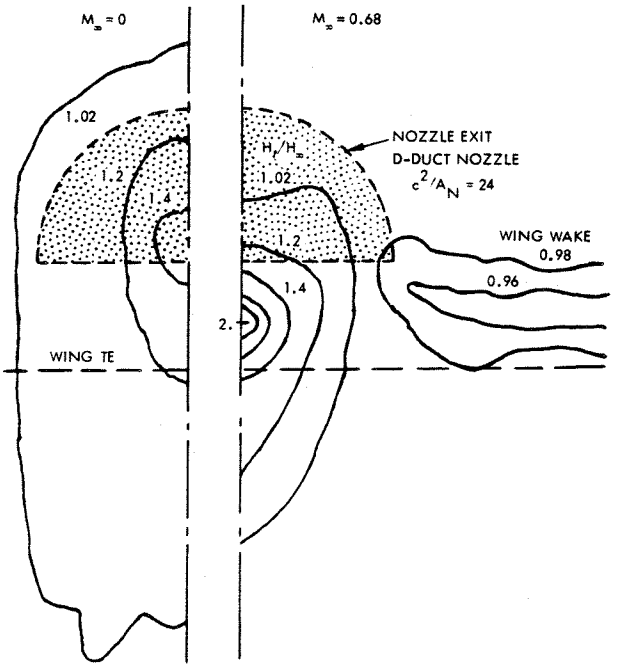

Figure 11. Comparison of Static and Wind-On Jet Isobars One Chord Length Behind Straight Wing, $H_j/P_\infty = 2.2$, $\alpha = 2.6^\circ$

turning-surface radius, R_w. As shown in Figure 12, both the pressure lift and drag can also be written as:

$$\Delta C_{D_j} = -\left[\frac{2h}{R_w} \cdot \frac{q_j}{q_\infty} \cdot \frac{\Delta\omega_e \Delta t}{S_{ref}}\right]$$

$$\Delta C_{L_j} = \left[\frac{2h}{R_w} \cdot \frac{q_j}{q_\infty} \cdot \frac{\Delta\omega_e \Delta_c}{S_{ref}}\right] \qquad (5)$$

$$\Delta C_{D_i} = C_T (1 - \cos\delta_j)$$

$$C_T = \frac{\rho_j A_j V_j^2}{q_\infty S_{REF}} = \frac{\rho_j h \Delta w_e V_j^2}{\frac{\rho_\infty V_\infty^2}{2} S_{REF}}$$

$$\cos\delta_j = \frac{R_w - \Delta t}{R_w}$$

$$\Delta C_{D_i} = \frac{\rho_j h \Delta w_e V_j^2}{\frac{\rho_\infty V_\infty^2}{2} S_{REF}} \left[1 - \left(\frac{R_w - \Delta t}{R_w}\right)\right]$$

$$\Delta C_{D_i} = 2\left[\frac{(\rho_j V_j^2)}{\rho_\infty V_\infty^2} \frac{(h \Delta w_e)}{S_{REF}} \frac{(-\Delta t)}{R_w}\right]$$

$$\Delta C_{D_i} = \left[\frac{2h}{R_w}\right]\left[\frac{q_j}{q_\infty}\right]\left[\frac{\Delta w_e \Delta t}{S_{REF}}\right]$$

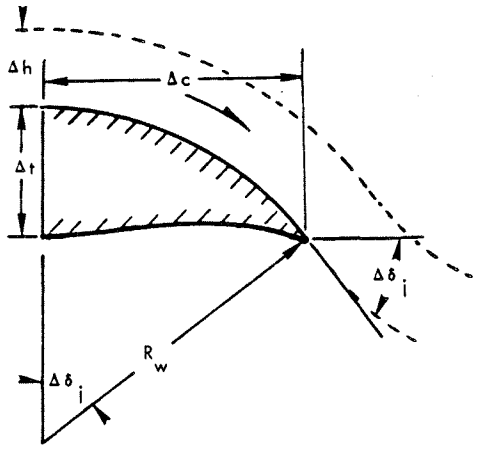

NOTE: BY SIMILAR DERIVATION:

$$\Delta C_{L_j} = C_T \sin\delta_j = \left|\frac{2h}{R_w}\right|\left|\frac{q_j}{q_\infty}\right|\left|\frac{\Delta w_e \Delta c}{S_{REF}}\right|$$

Figure 12. Derivation of Equivalent Expression for Jet-Turning Loads

From Reference 1, the parameter $2h/R_w$ is related to the maximum (negative) pressure coefficient generated statically on a curved surface by a thin, attached jet as

$$C_{p_j} = -\left(\frac{\Delta P}{q_j}\right) = -\left(\frac{2h}{R_w}\right) \qquad (6)$$

Even under wind-on test conditions, there appears to be some validity to the statically-derived equation (6) as demonstrated in the centerline pressures of Figure 13. A low nozzle pressure-ratio is used in this case to suppress the overlaying effects of the shocks on the pressure distribution trends. The C_p-levels as computed from:

$$C_p = \frac{2h}{R_w}\left(\frac{q_j}{q_\infty}\right) \qquad (7)$$

for the three nozzles are also shown. The maximum pressure difference between the D-Duct (AR = 2.5) and that of the aspect ratio 4 nozzle is about as predicted by this expression. However, the circular nozzle does not generate a negative pressure proportional to nozzle exit height due apparently to the inability of the thick, poorly-attached circular jet to follow the aft-wing surface; in this case, the round jet is blowing tangentially to the wing surface.

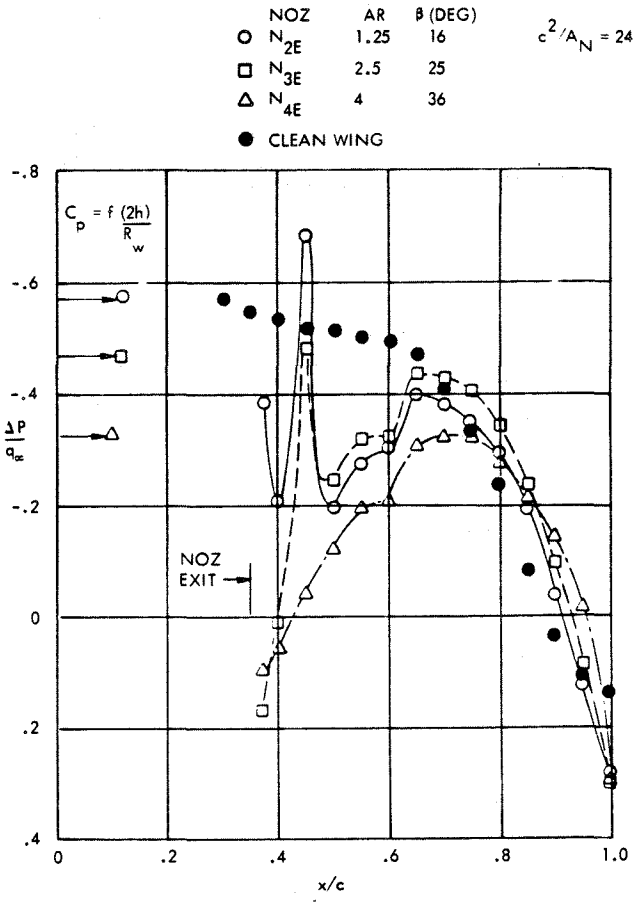

Figure 13. Effect of Nozzle Exit Shape on Jet Centerline Pressures, $\alpha = 2^\circ$, $M_\infty = 0.60$, $H_j/P_\infty = 1.4$

Equation (6) would also suggest that the ratio of jet-dynamic pressure to that of free-stream should be a correlating parameter on jet-centerline pressures regardless of Mach number or pressure ratio. Figure 14 shows that widely different test conditions provide about the same surface pressures, except for shock perturbations, when the jet dynamic pressure ratio is held constant. Additionally, a comparison of (a) and (b) in Figure 15 shows that, for a range of pressure ratios, normalizing C_p on q_j rather than q_∞, tends to collapse the centerline pressures except for the shock-induced excursions. As a result of such data it is concluded that jet dynamic pressure (or exit velocity ratio) is a major controlling parameter within the jet-scrubbing area irrespective of freestream Mach number or nozzle pressure ratio. This was also a basic conclusion in the high-speed tests of a similar USB system reported on in Reference 2.

To provide further insight into the jet-vectoring capability of the wing and for establishing a means of quantifying ΔC_{D_j}, centerline surface-pressure within the scrubbed area have been integrated in a dragwise direction to obtain an incremental drag coefficient, or:

$$\Delta C_{D_j} = \left[\int_{(x/c)_{exit}}^{x/c = 1} C_{pd} \left(\frac{z}{c}\right) \right] \Delta\eta \qquad (8)$$

where $\Delta\eta$ is the width of the nacelle exit normalized by the wing semi-span dimension. This expression provides a coefficient which assumes that jet centerline pressures remain essentially constant across the projected width of the nozzle exit. The assumption is not strictly correct, particularly for the more three-dimensional nozzle shapes (i.e. "D-Duct" and circular) for which centerline pressures generally exhibited a rapid a

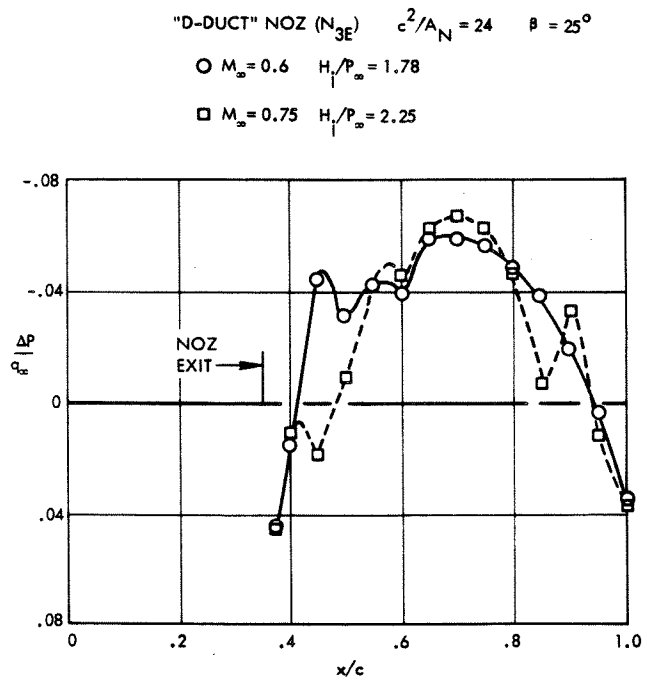

Figure 14. Jet Centerline Pressure Distributions at Constant $q_j/P_\infty = 2.3$, $\alpha = 2°$

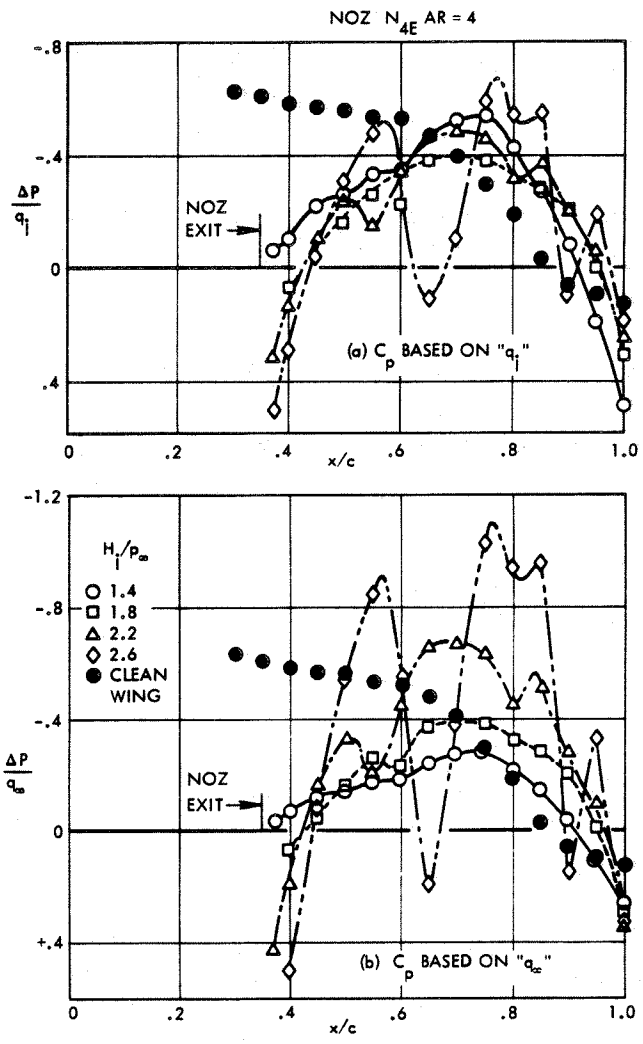

Figure 15. Effect of Nozzle Pressure Ratio on Jet Centerline Pressures, $\alpha = 3°$, $M_\infty = 0.68$

attenuation toward the edges of the jet. As noted in flow visualization studies, however, jet spreading beyond the limits of the nozzle projected width tended to remedy the major inadequacies of this assumption at least for the wider nozzles.

Examples typifying results of the integration process are given as a function of nozzle pressure ratio in Figures 16 and 17 for several medium-sized nozzles. Included with the nozzle-installed data are the pressure drag levels on the clean wing for the same aft areas. As noted, the nozzle-installed pressure drag approaches that of the clean wing at approximately the flow-through pressure ratio. To establish a drag increment relative to the clean wing, equation (4) would be modified to:

$$\Delta C_{D_j} = \eta \Delta C_T \ (1 - \cos \ (\alpha + \theta_j) \qquad (9)$$

where:

$$\Delta C_T = C_T - (C_T)_{\text{Flow-Through}}.$$

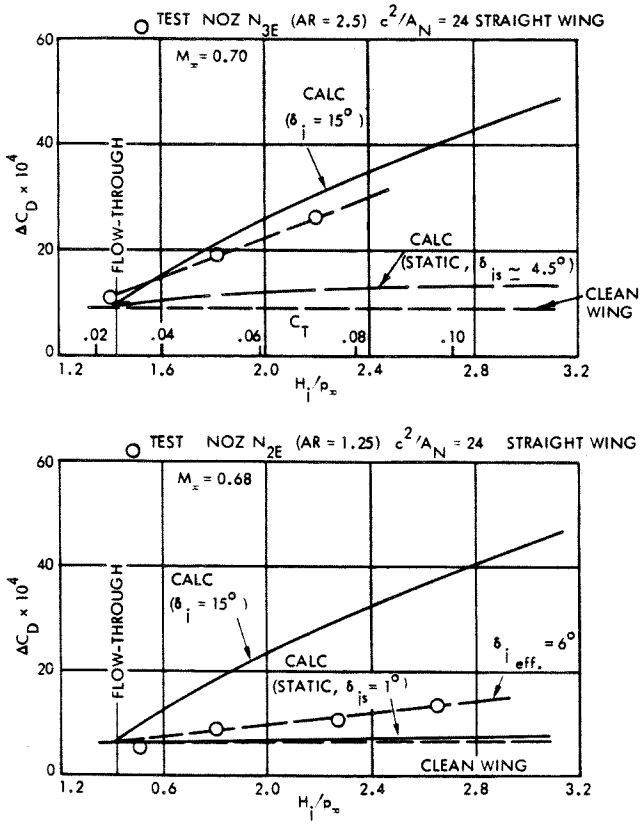

Figure 16. Variation of Scrubbed Area Pressure Drag with Pressure Ratio, $\alpha = 2^\circ$

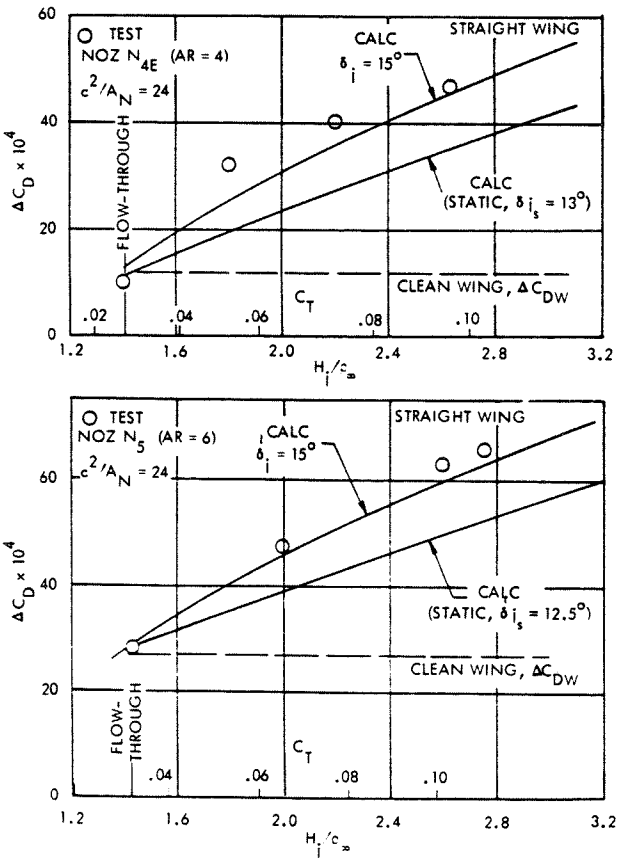

Figure 17. Variation of Scrubbed Area Pressure Drag with Pressure Ratio, $\alpha = 2^\circ$, $M_\infty = 0.68$

Equation (9) has been used to calculate the pressure drag increments shown in Figures 16 and 17 for each nacelle across the pressure ratio range. In these calculations, two values of δ_j were assumed: that found from the static testing and that approximating the aft-wing trailing-edge angle (≈15°). In all cases, except possibly the circular nacelle, the calculations are more consistent with the integrated pressure results when the 15° angle is used instead of the statically derived value. The "D-Duct" nozzle (AR = 2.5) data reflects a lower angle than that of the wing trailing-edge but still higher than from the static data. The circular nozzle (AR = 1.25), as would be expected, shows a very low effective vectoring angle but still significantly higher than the essentially zero capability indicated by the static test results. It should be noted here that, in the higher blowing range, abrupt pressure fluctuations due to the onset of wave patterns in the jet, created some difficulty in accurately performing the surface-pressure integrations. Therefore, the drag increments, and the representative deflection angle can be considered as only approximate at the higher pressure ratios. That other investigators have noted those same trends and effects is evidenced in Figure 18. In this figure, drag results of surface-pressure integrations from the present USB tests are compared to similar data behind an aspect ratio 3.3 nozzle, Reference 2; as noted, matching trends are obtained.

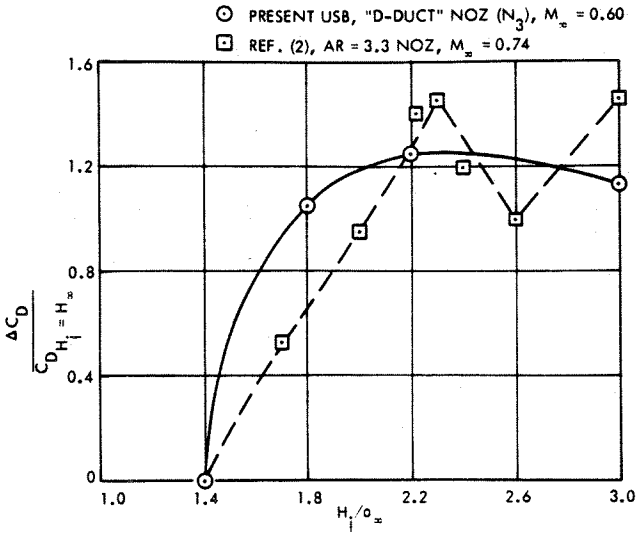

Figure 18. Comparison of Pressure Drag Developed in Scrubbed Area

Since the foregoing pressure integrations have been based on only that aft-facing segment of wing area immediately downstream of the nozzle exit, the possibility exists for full or partial recovery of the scrubbed area pressure drag by increased leading-edge suction on adjacent wing sections. Additionally, the leading-edge suction lost over that span of wing covered by the nacelle forebody should also be accounted for by this mechanism even at the flow-through pressure ratios. While modest reductions in adjacent leading-edge pressure (i.e. more negative) were noted as nozzle pressure ratio was advanced, these regions generally culminated in increasing strong shocks at the forward wing/nacelle-forebody junctures. It is believed, therefore, that due to the freestream Mach condition, coupled with displacement effects of the

highly three-dimensional nacelle forebody, a sufficient increase in leading-edge suction such as to overcome the foregoing aft-wing pressure drag would be highly unlikely. It is believed reasonable also, that the relatively modest loss in suction at the flow-through condition over that portion of the leading edge covered by the nacelle could be recovered by increased suction on adjacent sections. As will be indicated in a later section, this rationale appears to be warranted by the breakdown and correlation of the force data.

As a result of the foregoing analyses, a preliminary assessment of the jet pressure drag term, ΔC_{D_j}, would be based on equation (9) with the maximum value (at a given C_T) set by allowing δ_j to go to 15°. Based on a more complete analysis of the pressure tests, 15° would be applicable to the aspect ratio 4 and 6 nozzles while the circular nozzles would reflect a much lower angle of 6° - 7°; the "D-Duct" nozzle would fall intermediate to these two extremes or $\delta_j \approx 12° - 14°$.

Drag-Due-to-Lift, ΔC_{D_i}. The terminology "drag-due-to-lift" is used herein in lieu of "induced-drag" inasmuch as this component combines any α - (or C_L-) dependent drag term along with the potential flow induced drag. Thus, viscous effects, changes in shock position or strength, along with associated boundary-layer interactions varying with α are included in the drag-due-to-lift components. To quantify this term, plots of $C_{L_{TOT}}$ vs. $C_{D_{TOT}}$ were constructed for each nacelle at fixed pressure ratio and Mach number after removal of the calibrated thrust. The slopes of these polars defined an equivalent wing efficiency factor, "e_{noz}," which could be compared directly to that of the basic, clean wing. Typical results obtained from this conventional analysis are provided in Figures 19 and 20 for several straight-wing nacelle installations. The ordinate on these plots is defined as:

$$\frac{\Delta e}{e_w} = \frac{e_w - e_{noz}}{e_w} \qquad (10)$$

where "e_w" is the wing efficiency factor of the clean wing. A notable feature of these data is that there is a substantial drag-due-to-lift penalty incurred by the nacelle installation at the flow-through pressure ratio, $H_j/p_\infty \approx 1.4$. With the more three-dimensional nozzles (i.e. circular), this penalty is not significantly improved upon by blowing. With the wider, more two-dimensional nozzles, blowing reduces the initial penalty, possibly through boundary-layer entrainment from adjacent wing sections. In no case, however, was the penalty associated with initial nacelle installation fully recovered by blowing, at least for the test configurations studied. Using the effective wing efficiency factors, the drag-due-to-lift penalty is evaluated in the conventional manner as:

$$\Delta C_{D_i} = \frac{C_{L_{TOT}}^2}{\pi AR}\left(\frac{1}{e_{noz}} - \frac{1}{e_w}\right) \qquad (11)$$

Summation of Drag Components. The four major drag contributors, calculated by the foregoing, have been summed for comparison with the balance-measured nacelle drag increments. Figures 21 through 24 show the build-up of these calculated elements along with the total test values of ΔC_{D_N} for nozzles ranging in exit shape from circular

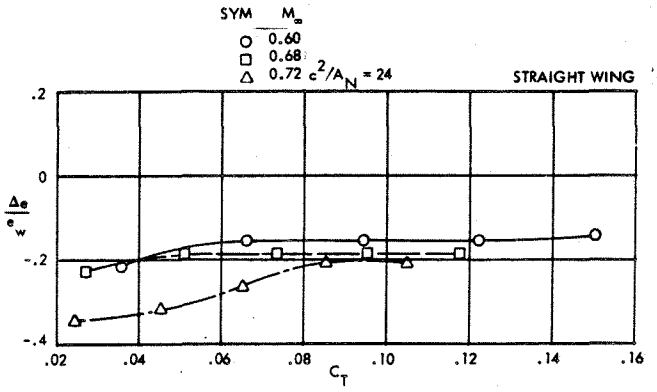

Figure 19. Variation of Effective Drag-Due-to-Lift Parameter with Thrust and Mach No., Nozzle N_{2_E}, Circular

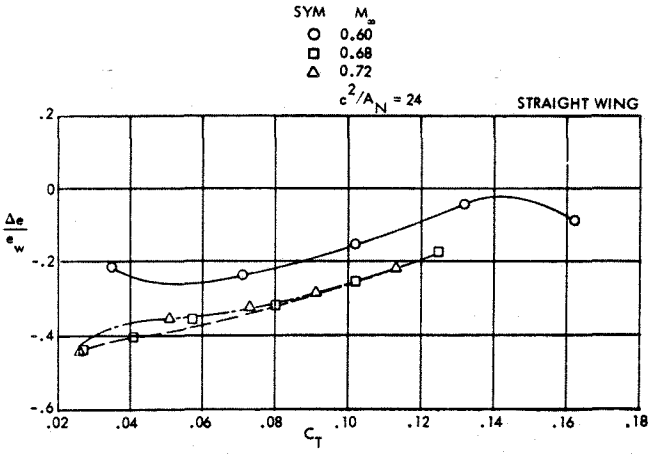

Figure 20. Variation of Effective Drag-Due-to-Lift Parameter with Thrust and Mach No., Nozzle N_5, AR = 6

to aspect ratio 5°; all data are for straight wing installations, a drag-rise Mach number of 0.68 and $C_{L_{TOT}} = 0.40$. Also shown are the values of effective jet-deflection angle used for approximating the jet-pressure drag term, ΔC_{D_j}. The "choked-nozzle" pressure of 1.89 generally define conditions where rapid changes in δ_j would be expected to occur; the value of δ_j used in the calculation and for which a reasonably close correlation with the measured data was obtained are shown on the plots. For the majority of the nacelles, the summed components were in good agreement with the measured data when jet angles, deduced from the pressure test results, were utilized for ΔC_{D_j}. For most of the nacelles, a total drag coefficient of $C_{D_N} = .0050 - .0060$ is obtained (AR = 1.25, 2.5, 4.0) for a $C_{L_{TOT}} = 0.4$ and a representative nozzle pressure ratio of 2.0. This penalty is high relative to conventionally-mounted, under-slung nacelles at the same operating conditions. In terms of aerodynamic interference (i.e. $\Delta C_{D_N} - \Delta C_{D_{NF}}$), the unrefined "D-Duct" installation incurs a penalty of about 10 percent of the combined wing, fuselage-nacelle drag. The aspect ratio 6 nozzle, Figure 24, on the other hand, exhibits a much higher drag penalty, due for the most part, to the poor integration of the nozzle/wing combination and the subsequent increase in drag-due-to-lift. It is apparent from these data that to minimize the cruise drag penalty, jet

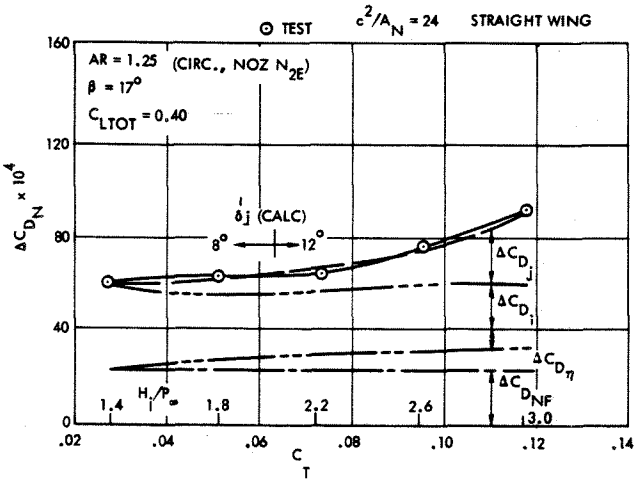

Figure 21. Incremental Nacelle Drag and Component Build-Up, $M_\infty = 0.68$

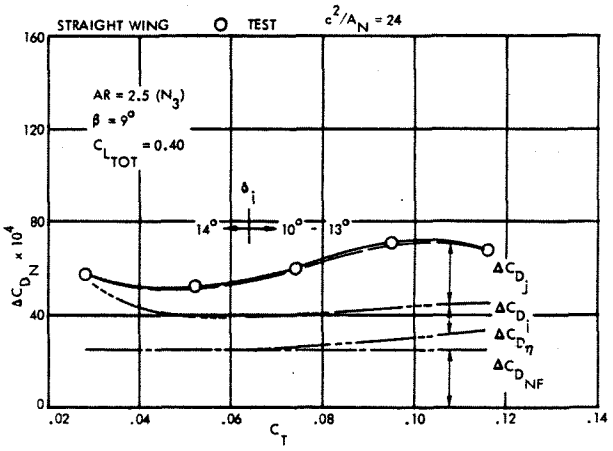

Figure 22. Incremental Nacelle Drag and Component Build-Up, $M_\infty = 0.68$

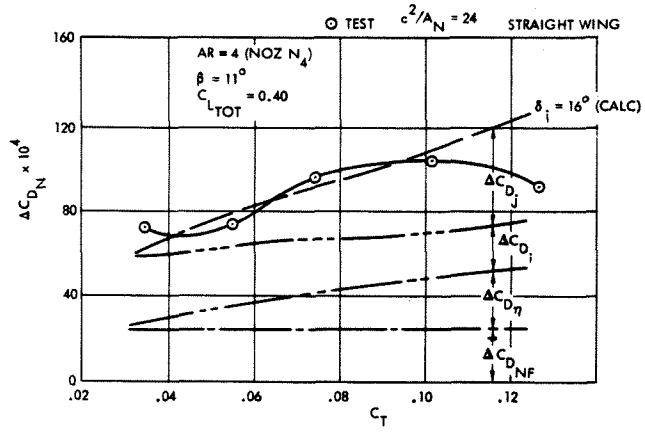

Figure 23. Incremental Nacelle Drag and Component Build-Up, $M_\infty = 0.68$

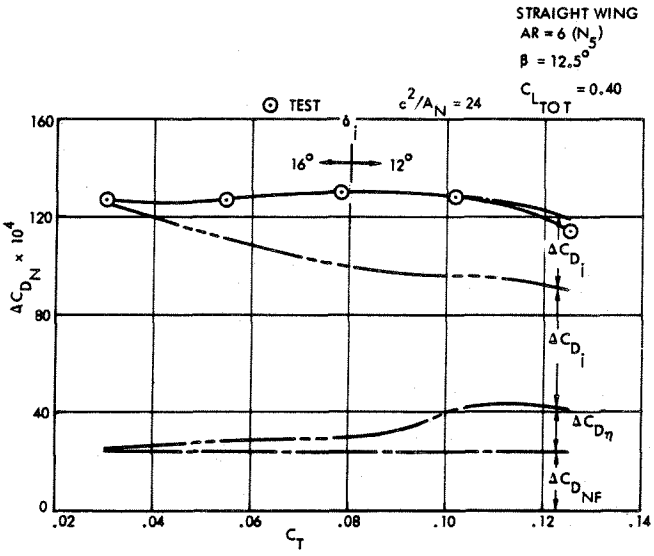

Figure 24. Incremental Nacelle Drag and Component Build-Up, $M_\infty = 0.68$

attachment to the wing should be prevented (reducing ΔC_{D_η} and ΔC_{D_j}) and, a contoured or blended nacelle/wing arrangement employed for improving the span-loading of the combined configuration (reducing ΔC_{D_i}).

Lift Increment Components. The total lift increment due to blowing, constant angle of attack, can be componentized as:

$$\Delta C_{L_{TOT}} = \Delta C_{L_N} + \Delta C_{L_{V/T}} + \Delta C_{L_\Gamma} \qquad (12)$$

where:

ΔC_{L_N} - change in basic wing lift accruing to the nacelle installation at flow-through pressure ratio ($H_j/P_\infty \approx 1.4$)

$\Delta C_{L_{V/T}}$ - lift component due to re-directed (or deflected) thrust at $H_j/P_\infty \gtrsim 1.4$.

ΔC_{L_Γ} - lift change due to increased wing circulation with blowing at $H_j/P_\infty > 1.4$.

In quantifying these components with the definitions given, test data may be used directly to evaluate ΔC_{L_N} and, $\Delta C_{L_{V/T}}$ can be obtained from:

$$\Delta C_{L_{V/T}} = \eta_T \, \Delta C_T \, (\sin\alpha + \delta_j) \qquad (13)$$

using the same rationale as pertaining to equation (9). In keeping with the nacelle drag build-up, the δ_j term in equation (13) would be approximately 15° except for the circular exit shapes exhibiting the lower deflection angles (6° - 7°). The ΔC_{L_Γ} term would be represented by the remainder of the total lift-due-to-thrust after summation of the first two terms. A breakdown of the measured total lift by this process is shown in Figure 25 for several representative nozzle configurations at $M_\infty = 0.68$ and $\alpha = 3°$. In these data, the basic clean wing-plus-fuselage lift is shown on the left. At the flow-through pressure ratio ($H_j/P_\infty \approx 1.4$) the total measured lift indicates a small negative lift

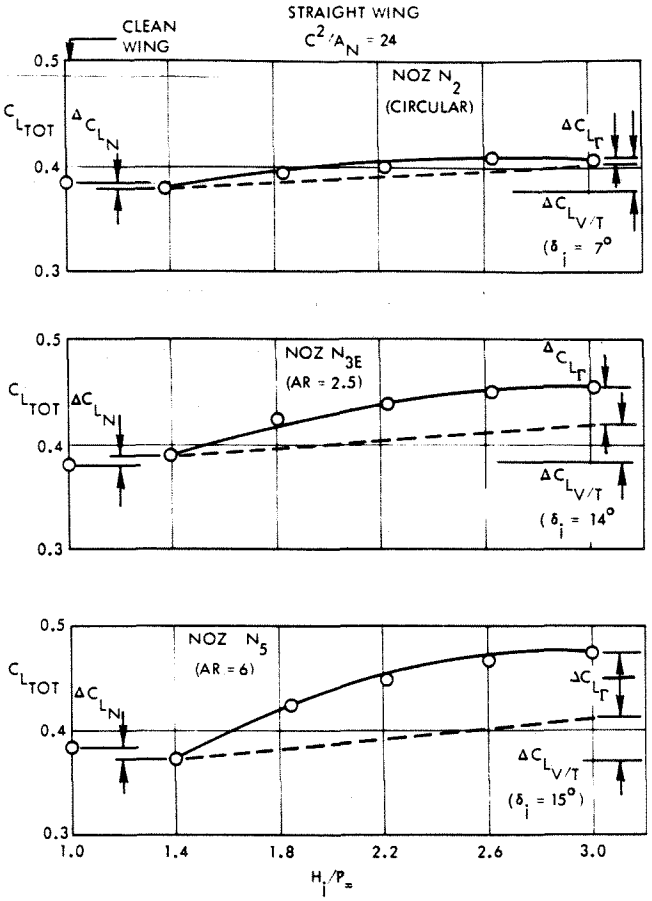

Figure 25. Components of Total Lift Coefficient, $M_\infty = 0.68$, $\alpha = 3^\circ$

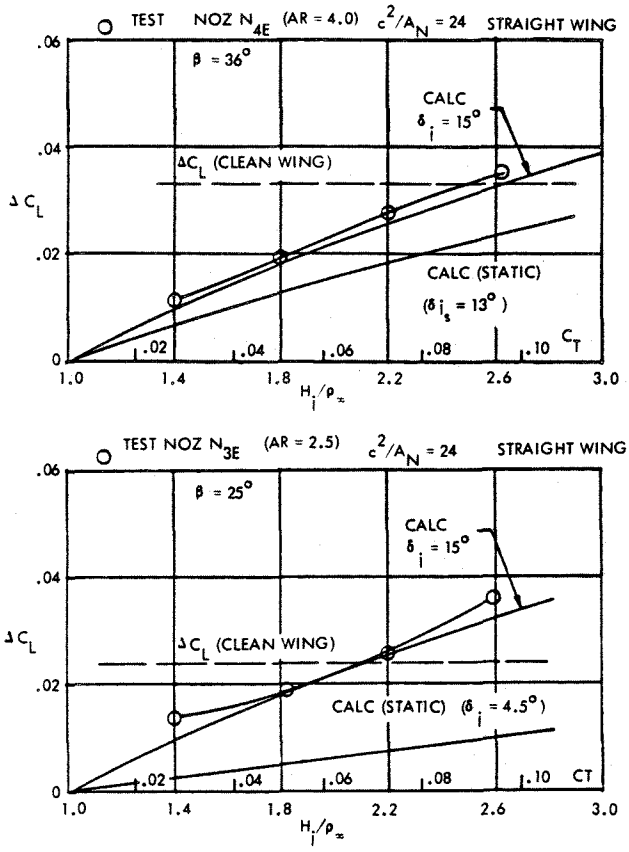

Figure 26. Integrated Lift Developed in Scrubbed Area with Blowing, $\alpha = 2^\circ$, $M_\infty = 0.70$

component representative of ΔC_{L_N}; this was true for most of the nozzles tested. After accounting for the direct-thrust increment, the remaining or circulation lift is shown to increase rapidly with nozzle aspect ratio as would be anticipated. The general trend of the total lift is a rapid increase in lift with blowing with a leveling-off at the high blowing rate. The lift trends did not show quite the same fluctuations in level as did the drag in the high blowing range. Pressure data indicated that aft-wing pressure changes due to jet attachment/ detachment represented a much smaller percentage of the section lift than was the case for the pressure drag.

To obtain additional insight into the composition of the total lift increment, the surface pressures within the scrubbed region were integrated under the same assumptions as noted for the drag components. Results from this process are shown in Figure 26 as a function of nozzle pressure ratio. These data show that, when considering only the scrubbed area downstream of the nozzle exit, lift is reduced upon nozzle installation below that carried by the clean wing. This is particularly true when the high boattail angle (36°), aspect ratio 4 nozzle is installed. As blowing increases, lift in the scrubbed area recovers toward the clean-wing value. Lift behind the "D-Duct" nozzle is not initially suppressed as strongly as that of the aspect ratio 4 configuration due to a much lower boattail angle of 25 degrees. At the high blowing rate, lift is shown to exceed that carried on the clean wing. Also shown on Figure 26 is the lift increment calculated by equation (13) using several values of the jet deflection angle, δ_j. As in the drag discussions, a value for δ_j approaching that of the wing trailing-edge is more compatible with the integrated pressure than the statically-derived values, particularly for the high aspect ratio nozzles.

A comparison of the data of Figures 25 and 26 for the "D-Duct" nozzle, N_{3E}, show the integrated lift increment generated by scrubbed area pressures is substantially less than the balance-measured lift increment due to blowing. Thus, a substantial amount of jet-induced lift must be carried by adjacent wing sections. Some indication of this is evidenced by the flow-survey data of Figure 10 which shows that the maximum trailing-edge injection angle occurs just beyond the boundary defined by the projected nozzle width; the lift on these adjacent sections should increase accordingly. This effect, coupled with localized boundary-layer entrainment on the adjacent wing, is believed to account for the additional system lift as evidenced by the force data.

In the general study of the total lift increment breakdown, a simplified jet-flap theory (References 3 through 5) was applied to reproduce the effects

of power. This theory, correcting for limited span blowing and compressibility provided an expression for total lift as:

$$C_{L_{TOT}} = F\left(1 + \frac{t/c}{\beta}\right)\left[\lambda C_{\ell_\delta} \cdot \frac{\Delta\delta}{\beta} + \gamma C_{\ell_\alpha} \cdot \frac{\Delta\alpha}{\beta}\right] - \frac{t/c}{\beta} C_T \left(\frac{\Delta\alpha}{\beta} + \frac{\Delta\delta}{\beta}\right)$$

where

$$F = \frac{\beta\, AR + 2\beta C_\mu/\pi}{\beta AR + 2 + .604\sqrt{\beta C_\mu} + .0876\,\beta C_\mu}$$

$$\lambda = \frac{S'}{Sw} = \frac{\text{Blown Area}}{\text{Total Area}}$$

$$\gamma = \frac{S' C_{\ell_\alpha} - (Sw - S')\,(C_{\ell_\alpha})_{C_\mu = 0}}{Sw\, C_{\ell_\alpha}}$$

$$C_{\ell_\delta} = \left[4\pi\beta C_\mu\,(1 + .151\sqrt{\beta C_\mu} + .139\,\beta C_\mu)\right]^{\frac{1}{2}}$$

$$C_{\ell_\alpha} = 2\pi(1 + 0.151\sqrt{\beta C_\mu} + 0.219\,\beta C_\mu)$$

$$\beta = \sqrt{1 - M_\infty^2}$$

$C_{\ell_\alpha} = \frac{\partial C_\ell}{\partial \alpha}$, two-dimensional lift-curve slope

$C_{\ell_\delta} = \frac{\partial C_\ell}{\partial \alpha}$, two-dimensional lift due to (jet) flap deflection

Sample calculations performed for several USB test configurations are compared to experimental results in Figures 27 and 28. In the calculations, an experimental value of C_{ℓ_α}, derived from USB two-dimensional pressure tests, was used in lieu of the foregoing theoretical expression. As such, calculated data apply primarily to the incremental effects of power on lift. In all cases, correlations were found to be excellent as long as jet angles of about 15° was used for the majority of the wide nozzles and about 6° used for the circular exit shapes.

4.0 Nacelle Geometric Effects

The bulk of the experimental data, inclusive of the foregoing components of the lift and drag increments, have been employed to study nacelle geometric variables as related to cruise aerodynamics. Some of the more significant effects are discussed below.

Nozzle Aspect Ratio Effects

Due to the importance of nozzle exit aspect ratio as a meaningful variable to both low and high-speed design, drag trends as a function of this variable are emphasized.

Total Nacelle Drag. Figure 29 shows the effect of nozzle exit aspect ratio on the total nacelle drag increment at $M_\infty = 0.68$ over a range of nozzle thrust coefficients. The drag is given in ratio form normalized to the drag of the circular nozzle.

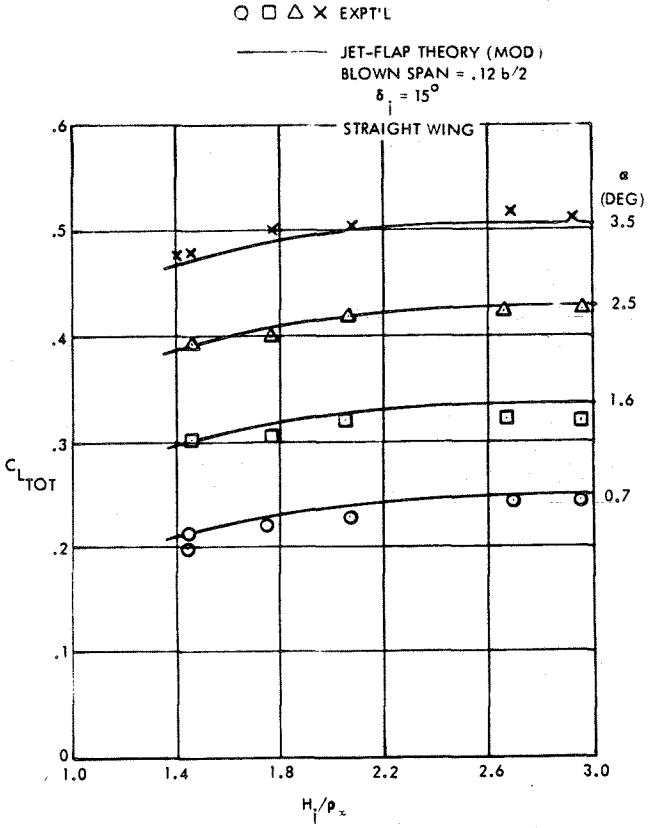

Figure 27. Comparison of USB Test Results with Modified Jet-Flap Theory, Noz N_{3_E}, AR = 2.5, $M_\infty = 0.68$

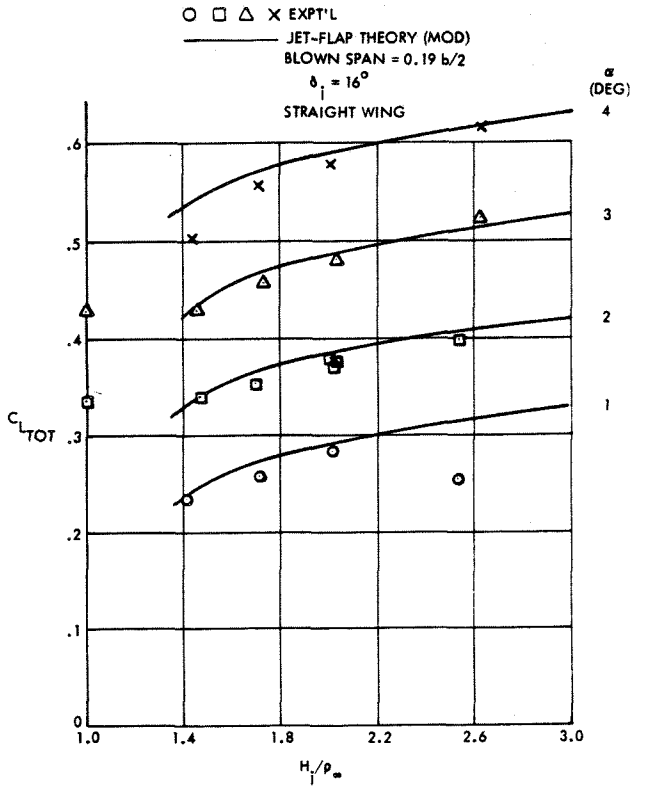

Figure 28. Comparison of USB Test Results with Modified Jet-Flap Theory, Noz N_5, AR = 6, $M_\infty = 0.68$

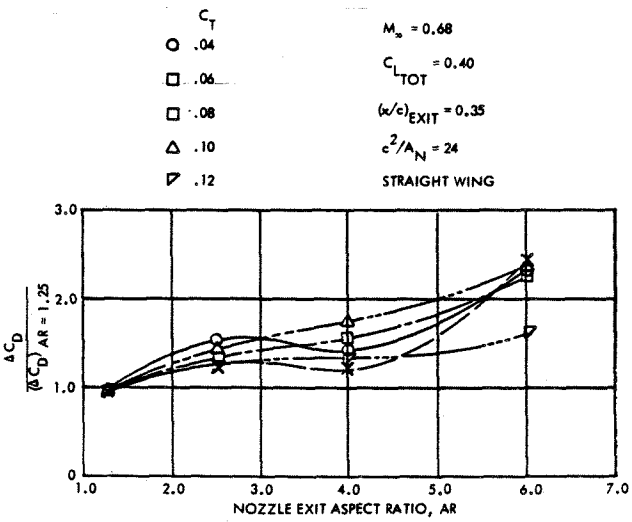

Figure 29. Effect of Nozzle Aspect Ratio on Nacelle Drag

While the general trend is an increase in drag with nozzle width, the design gross thrust (i.e. C_T) also needs to be considered in selecting a candidate, low-drag nozzle design. Additionally, while the circular nozzle shows the least cruise drag penalty in these data, recognition of targeted high-lift performance could readily bias a compromised selection to a somewhat higher aspect ratio such as the "D-Duct."

For a typical cruise gross thrust coefficient of 0.08 and higher, the data clearly indicate, however, that the lower the nozzle aspect ratio, the better the potential cruise performance for the configurations tested.

Drag-Due-to-Lift. A primary reason for the lower aspect ratio nozzles showing better cruise performance than the high aspect ratio installations is demonstrated in Figure 30. Drag-due-to-lift for $C_{L_{TOT}} = 0.4$, is plotted as a function of nozzle exit aspect ratio for the two boattail-angle series of medium-sized nozzles. For the short, high boattail-angle configurations, there is a definite "bucket" in the lift-dependent drag at an aspect ratio approaching that of the "D-Duct" installation at all blowing rates. The aspect ratio 4 nozzle (N_{4E}), with an unrealistically high boattail angle of 36°, is penalized heavily by lift-dependent drag. A similar trend, but without a pronounced drag minimum, is shown for the low-boattail-angle nozzle series. These nozzles were designed with a short, straight section ahead of the nozzle exit in order to minimize the jet-impingement on the wing surface. This feature appeared to be particularly effective in suppressing jet-attachment by the wide, thin nozzles at high blowing rates

Nozzle Boattail Angle Effects. The angle between the nacelle upper-surface centerline at the exit and the wing chord plane, as used herein, is the boattail angle, β. Across the range of exit shapes tested, this angle varied from about 6° to a maximum of about 36°. In general, the lower angles represented circular nozzle designs with the higher angles required by the wider, high aspect ratio nacelles. For a given nozzle aspect ratio, this angle was also varied by changing the nacelle

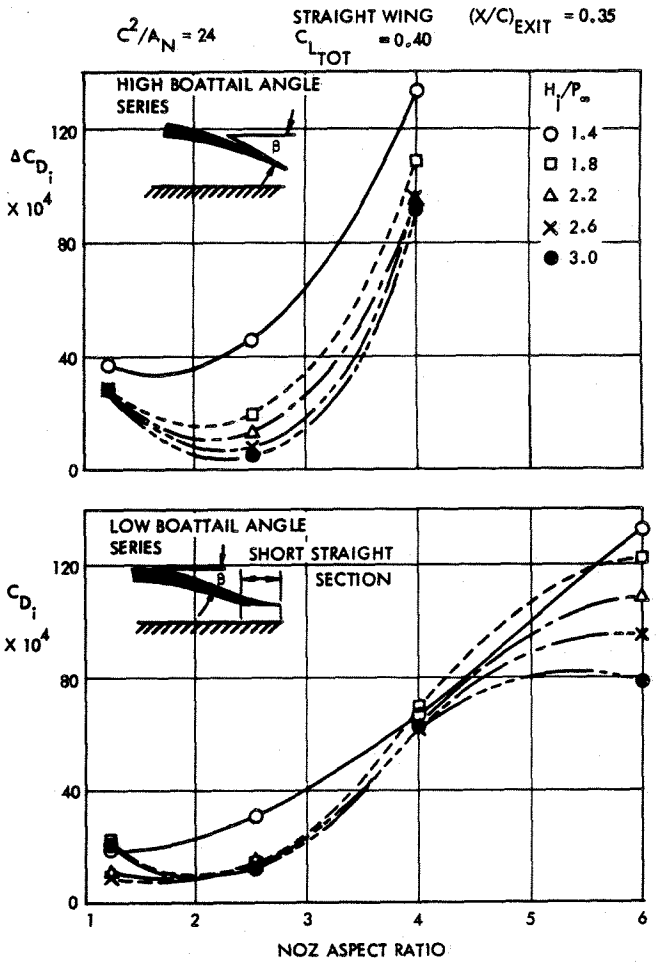

Figure 30. Effect of Nozzle Exit Aspect Ratio on Lift-Dependent Drag, $M_\infty = 0.68$

forebody length. In an attempt to define a limiting angle from a cruise standpoint, the data of Figure 31 have been prepared. Test results are shown in a drag-ratio-form with the denominator representing a circular nozzle with $\beta \approx 6°$. Below $\beta \approx 25°$ the trends are not completely uniform due, it is believed, to variations in the effectiveness of the wing/ nacelle filleting provided. Above 25°, however, the sharp increase in drag suggests that about 25° represents a maximum design value of β if severe boattail separation effects are to be avoided. It is also noted that as C_T increases, the drag ratio at high values of β diminishes in value as the jet tends to suppress some of the separation through a pumping effect.

Effect of Multiple Nacelles. Figure 32 compares the nacelle drag increment of a four-engine, swept-wing configuration to that of a two-engine design, both with small "D-Duct" nozzles (N_8) at several pressure ratios. As presented, the friction drag ($\Delta C_{D_{NF}}$) of the nacelles has been removed from the drag increment. Also shown is a drag level derived by taking one-half of the four-engine increment for comparison to the two-engine version. At both of the representative pressure ratios, the data show that the drag does not scale proportionally with the number of engines with the two-engine configuration showing a higher relative interference drag than does the four-engine case. In the drag-due-

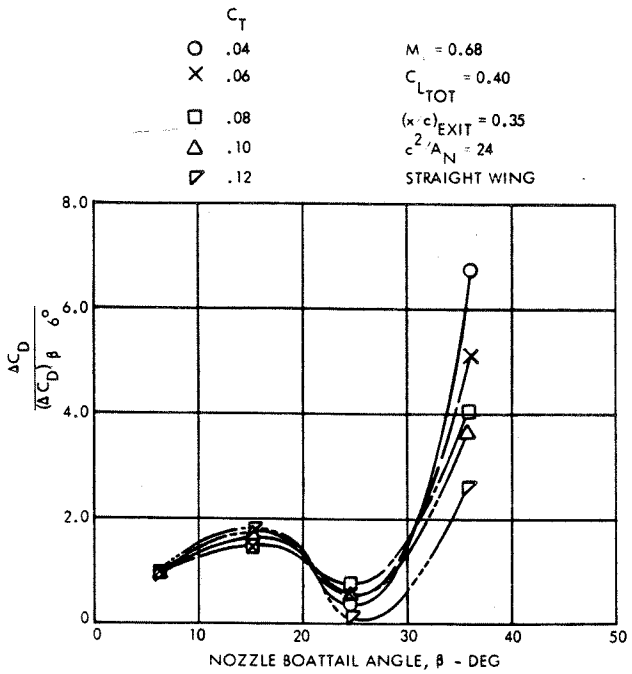

Figure 31. Effect of Nacelle Boattail Angle on Nacelle Drag

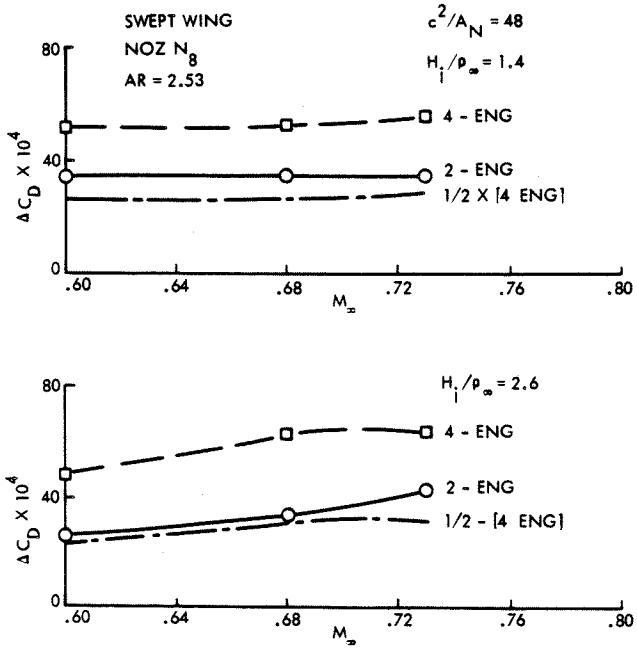

Figure 32. Effect of Multiple Engine Installation on Drag, $C_{L_{TOT}}$ = 0.40, Swept Wing, D-Duct Nozzle

to-lift analysis it was found that while this penalty is larger for the four-engine version, it is not doubly so. Additionally, the drag build-up showed that, in general, the four-engine configuration reflects slightly lower turning angles than the two-engine counterpart thus producing slightly less pressure drag. Further evidence of this difference is shown in Figure 33 where the lift-due-to blowing is presented for the two cases at $M_\infty = 0.73$. Except at the highest pressure ratio, the total lift of the 4-engine configuration is less than that of the two-engine with the lift trend of

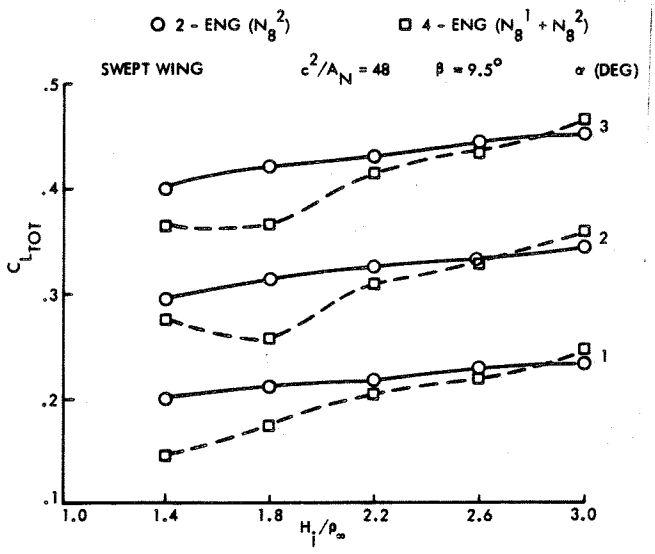

Figure 33. Comparison of Lift-Due-to-Blowing for 2-Engine and 4-Engine Configurations, "D-Duct" Nacelle, Swept Wing, $M_\infty = 0.73$

the former showing intermittent attachment of the jet in the lower blowing range. Note also in these data, that the four-engine case is producing twice as much thrust as its two-engine counterpart. Although the jets are widely spaced, it is believed that the two jets, operating in proximity to each other with both exits at a constant x/c = 0.20, produce a mutual interference which tends to suppress jet attachment.

5.0 Conclusions

Representative results have been presented on an experimentally-based study of the USB-system at cruise. Conclusions drawn must reflect the "data-base" nature of the experimental work in which relatively unrefined models and a broadly-spaced test matrix were necessary features. Specific conclusions attendant to this study have included the following:

1. In the unrefined state, the total drag penalty of typical USB-nacelle configuration, under transonic-cruise, powered conditions, can be exceptionally high by conventional propulsion-installation standards.

2. The major drag producing phenomena in the general case, appears to be

- o a jet-scrubbing effect on the aft-wing surface
- o the conventional aerodynamic friction drag of the nacelle/nozzle and associated external hardware
- o a pressure-drag component representing deflection of the jet over the aft-wing surface
- o a drag-due-to-lift component inclusive of all lift-related transonic phenomena under powered-model conditions
- o a potential drag penalty reflecting excessive nozzle boattail angles which promote local flow separation.

3. The major drag components are generally identifiable by force and surface-pressure measurements of powered models tested under both static and wind-on conditions.

4. Scrubbing losses tend to increase with nozzle two-dimensionality (i.e. increasing nozzle aspect ratio) and nozzle pressure ratio.

5. Pressure drag, tending to increase with nozzle width, aft-wing camber, angle-of-attack, and nozzle pressure-ratio appears to be moderated by the jet shock formations at high nozzle pressure ratios.

6. Highly three-dimensional jets, such as a circular shape, can also show significant amounts of pressure drag at cruise conditions even under partial jet-attachment conditions.

7. For moderate and high nozzle aspect ratios ($AR \geq 2.5$), effective jet deflection by the aft wing surface appears from correlation studies to be within several degrees of the wing upper-surface at the trailing edge.

8. Total lift performance at constant angle-of-attack is improved by increasing nozzle exit aspect ratio - typical values at a nozzle pressure ratio of 3.0 are $\Delta C_L \simeq .03$ for a circular nozzle and about $\Delta C_L \simeq 0.10$ for an aspect ratio 6.0 nozzle.

9. A semi-circular ("D-Duct") nozzle ($AR = 2.5$) represents a reasonable compromise between good cruise and potentially-favorable high-lift performance.

10. Nozzle boattail angles in excess of about 25 degrees may cause significant drag penalties due to local flow separation.

11. On a multi-jet configuration with nacelles spaced 1.6 D apart, both lift and drag increments due to blowing are diminished by an apparent mutual interference between the adjacent jets.

Nomenclature

A_N	nozzle exit area, cm^2 ($in.^2$)
AR	nozzle exit aspect ratio
b	wing span, cm (in.)
c	wing chord, cm (in.)
$C_{L_{TOT}}$	total (or measured) lift coefficient
$C_{D_{TOT}}$	total (or measured) drag coefficient
C_T	thrust coefficient, $T/q_\infty S_{REF}$
ΔC_{D_N}	total drag coefficient due to nacelle
ΔC_{L_N}	total lift coefficient due to nacelle
D	nacelle diameter, cm (in.)
e_w	basic wing "efficiency factor"
e_{noz}	wing plus nacelle "efficiency factor"
h	jet height, cm (in.)
H_j	jet total pressure, N/m^2 ($lb/in.^2$)
H_∞	freestream total pressure, N/m^2 ($lb/in.^2$)
M_∞	freestream Mach number
P_∞	freestream static pressure, N/m^2 (lb/in^2)
ΔP	static pressure increment, N/m^2 ($lb/in.^2$)
q_∞	freestream dynamic pressure, N/m^2 (lb/in^2)
q_j	jet dynamic pressure, N/m^2 ($lb/in.^2$)
S_{REF}	reference area, cm^2 ($in.^2$)
$T_{INSTALL}$	installed thrust, N (lb.)
T_{ISOL}	thrust of isolated nacelle, N (lb.)
Δw_e	"effective" jet width, cm (in.)
ΔY	dimension in spanwise direction, cm (in.)
α	angle of attack, degrees
δ_j	jet deflection angle, degrees
η_T	thrust efficiency factor, $T_{INSTALL}/T_{ISOL}$
$\Delta\eta$	$\Delta Y/(b/2)$

Subscripts

s	static condition
ℓ	local
∞	freestream
N	nacelle

5.0 References

1. Roderick, W. E. B.: Use of the Coanda Effect for the Deflection of Jet Sheets Over Smoothly Curved Surfaces. Institute of Aerophysics, University of Toronto, September 1961.

2. Kettle, D. J.; Kurn, A. G.; and Bagley, J. A.: Exploratory Tests of a Forward-Mounted Over Wing Engine Installation. CP No. 1207, R.A.E., Farnborough, 1972.

3. Spence, D. A.: The Lift Coefficient of a Thin Jet-Flapped Wing. Proc. Roy. Soc. Series A, Vol. 121, 1956.

4. McCormick, B. W.: *Aerodynamics of V/STOL Flight*. Chapter 7, Academic Press, New York, 1967.

5. Elzwig, S.: Subsonic Similarity Rule for Jet Flapped Airfoil. *Journal of Aircraft*, Vol. 8, No. 9, September 1971.